Monthly Notices
of the
ROYAL ASTRONOMICAL SOCIETY

MNRAS **480,** 5550–5559 (2018) doi:10.1093/mnras/sty2049

Celestial mechanics and polarization optics of the Kordylewski dust cloud in the Earth–Moon Lagrange point L5 – I. Three-dimensional celestial mechanical modelling of dust cloud formation

Judit Slíz-Balogh,[1,2] András Barta[2,3] and Gábor Horváth[2]★

[1]*Department of Astronomy, ELTE Eötvös Loránd University, H-1117 Budapest, Pázmány sétány 1, Hungary*
[2]*Environmental Optics Laboratory, Department of Biological Physics, ELTE Eötvös Loránd University, H-1117 Budapest, Pázmány sétány 1, Hungary*
[3]*Estrato Research and Development Ltd, H-1124 Németvölgyi út 91/c, Budapest, Hungary*

Accepted 2018 July 16. Received 2018 July 07; in original form 2018 May 4

ABSTRACT

Since the discovery in 1772 of the triangular Lagrange points L4 and L5 in the gravitational field of two bodies moving under the sole influence of mutual gravitational forces, astronomers have found a large number of minor celestial bodies around these points of the Sun–Jupiter, Sun–Earth, Sun–Mars and Sun–Neptune systems. The L4 and L5 points of the Earth and Moon might be empty due to the gravitational perturbation of the Sun. However, in 1961, the Polish astronomer, Kazimierz Kordylewski found two bright patches near the L5 point, which might refer to an accumulation of interplanetary particles. Since then, this formation has been called the Kordylewski dust cloud (KDC). Until now, only a very few computer simulations have studied the formation and characteristics of the KDC. To fill this gap, we have investigated a three-dimensional four-body problem consisting of the Sun, Earth, Moon and one test particle, 1 860 000 times separately. We mapped the size and shape of the conglomerate of particles that have not escaped from the system sooner than an integration time of 3650 d around L5. Polarimetric observations of a possible KDC around L5 will be presented in a following second part to this paper.

Key words: polarization – instrumentation: polarimeters – methods: observational – celestial mechanics – Earth – Moon.

1 INTRODUCTION

In 1767, Euler discovered three unstable collinear points (L1, L2 and L3). Later, in 1772, Lagrange found two triangular points (L4 and L5) in the gravitational field of two bodies moving under the sole influence of mutual gravitational forces (Szebehely 1967). In the three-body problem of celestial mechanics, the L4 and L5 Lagrange points are stable in linear approximation, if the mass ratio $Q = m_{\rm smaller}/m_{\rm larger}$ of the two primaries is smaller than $Q* = 0.0385$ (Murray & Dermott 1999). Astronomers have found a large number of minor celestial bodies around these points of the planets of our Solar system and the Sun. The most well-known are the Greek and Trojan minor planets around the L4 and L5 points of the Sun–Jupiter system (Schwarz & Dvorak 2012; Schwarz, Funk & Bazsó 2015). Minor planets have also been found around the triangular Lagrange points of the Sun–Earth (John, Graham & Abell 2015), Sun–Mars (Christou 2017) and Sun–Neptune systems (Sheppard &Trujillo 2006).

What about the vicinities of the Lagrange points L4 and L5 of the Earth and Moon? Because the mass ratio $Q = m_{\rm Moon}/m_{\rm Earth} = 0.0123$ of the Moon and Earth is smaller than $Q* = 0.0385$, the L4 and L5 points are theoretically stable. Thus, interplanetary particles with appropriate velocities could be trapped by them. In spite of this fact, they might be empty due to the gravitational perturbation of the Sun. Taking into account the perturbation of the Sun, the orbits in the vicinity of the L5 point have been computationally investigated in two dimensions (Slíz, Süli & Kovács 2015; Slíz, Kovács & Süli 2017). According to the results of these simulations, if test particles start from the vicinity of the L5 point, their motion will be chaotic. This chaos is transient, and there are many trajectories that do not leave the system even for 10^6 d, and long-existing (for 30–50 yr) islands form around L5. Thus, although the gravitational perturbation of the Sun really sweeps out many trajectories from the L5 point on an astronomical time-scale, on a shorter time-scale there are also many long-existing trajectories.

In 1961, the Polish astronomer, Kazimierz Kordylewski found two bright patches near the L5 point, which might refer to an accumulation of dust particles (Kordylewski 1961). Since then, this hypothetical formation has been called the Kordylewski dust cloud

★ E-mail: gh@arago.elte.hu

(KDC). Until now, only a very few computer simulations have studied the formation and characteristics of the KDC (Slíz et al. 2015, 2017; Salnikova, Stepanov & Shuvalova 2018). To fill this gap, here we investigate a three-dimensional (3D) four-body problem consisting of three massive bodies – the Sun, the Earth and the Moon (primaries) – and a low-mass test (dust) particle, 1 860 000 times separately. Our aim was to map the size and shape of the conglomerate of particles that have not escaped from the system sooner than a given integration time around L5. Polarimetric observations of a possible KDC around L5 will be presented in a following second part to this paper (Slíz-Balogh, Barta & Horváth 2018).

2 MODELS AND METHODS

We used a 3D barycentric four-body model consisting of the Sun, Earth, Moon and a test particle (called simply 'particle' hereafter) near the L5 point of the Earth–Moon system (Fig. 1). The initial positions and velocities of the Sun, Earth and Moon were taken from the freely available NASA Jet Propulsion Laboratory (JPL) data base (https://ssd.jpl.nasa.gov/horizons.cgi) in the ecliptic coordinate system with Cartesian coordinates relative to the Solar system barycentre. These coordinates (and also the input coordinates of the L5 point) were converted to Sun–Earth–Moon–particle barycentric ecliptic coordinates. All calculations were performed in this 3D Sun–Earth–Moon–particle barycentric ecliptic coordinate system, while the representations were made in a geocentric ecliptic coordinate system for the sake of better visualization.

Because this is a 3D model, the computation of the coordinates of the L5 point was performed as follows.

(i) Based on the Moon's orbital data obtained from the NASA JPL data base, the longitude of the ascending node and the inclination with respect to the Earth's equator were calculated.

(ii) The ecliptic coordinates of the Moon were converted into equatorial coordinates, and then they were rotated twice: first, with the longitude of the ascending node about the z-axis, and then with the inclination relative to the Earth's equator into the equatorial plane about the x-axis.

(iii) In the equatorial plane, the position and velocity of the L5 point were calculated by rotating the Moon's coordinates 60° clockwise.

(iv) Finally, these coordinates were rotated back: first, with the inclination relative to the Earth's equator into the equatorial plane about the x-axis, and then with the longitude of the ascending node about the z-axis.

The potential energy U and motion equations of the Sun–Earth–Moon–particle system are the following:

$$U = -\gamma \sum_{i=1, i\neq j}^{4} \frac{m_i m_j}{r_{ij}},$$
$$r_{ij} = \sqrt{(x_i - x_j)^2 + (y_i - y_j)^2 + (z_i - z_j)^2}, \quad (1)$$

$$m_i\,\ddot{x}_i = -\frac{\partial U}{\partial x_i}, \qquad m_i\,\ddot{y}_i = -\frac{\partial U}{\partial y_i}, \qquad m_i\,\ddot{z}_i = -\frac{\partial U}{\partial z_i},$$
$$i = 1,\ 2,\ 3,\ 4. \quad (2)$$

Here, $\gamma = 6.674 \times 10^{-11}$ m^3 kg^{-1} s^{-2} is the universal gravitational constant, m_1, m_2, m_3 and m_4 are the masses of the Sun, the Earth, the Moon and the particle, respectively, and r_{12}, r_{13}, r_{14}, r_{23}, r_{24} and r_{34} are the distances between the Sun–Earth, Sun–Moon, Sun–particle, Earth–Moon, Earth–particle and Moon–particle, respectively, in the x–y–z barycentric ecliptic coordinate system (Fig. 1). The second-order non-linear differential equations (2), obtained by derivation from equation (1), were converted into a system of first-order differential equations, which were solved with an appropriate Runge–Kutta method. The motion equations were implemented in a dimensionless form, where the characteristic length unit is 1 au = 149 597 870.66 km and the time unit is 86 400 s (= 1 d). The computational method was an adaptive step size Runge–Kutta–Fehlberg integrator of order 7(8) (Fehlberg 1968) in which the actual step size is determined according to the desired accuracy $\varepsilon = 10^{-16}$ (= tolerated local error per unit step).

A particle is considered as trapped (in fact, non-escaped), if in 3650 d it does not leave the spherical shell $0.5r_0 \leq D \leq 1.5r_0$ with

$$r_0 = \sqrt{(x_0 - x_{E0})^2 + (y_0 - y_{E0})^2 + (z_0 - z_{E0})^2},$$

where x_0, y_0, z_0, x_{E0}, y_{E0} and z_{E0} are the initial coordinates of the particle and the Earth at starting time t_0, and D is the thickness of the shell. If we want to model the KDC around the Lagrange point L5, then, of course, it is not enough to start the particles at a single t_0. In principle, continuous trapping should be modelled in a medium with unknown particle density and velocity. Instead of this, we used the following approach. For a given t_0, the motion equations were solved for 1 860 000 particles, the starting positions and velocities of which were distributed in the phase space in the vicinity domain V of the L5 point (Table 1). The V domain was divided into 41 equal parts in the x, y and z ranges, and three equal parts in the v_x, v_y and v_z ranges. The trapped (non-escaped) particles constitute a 'particular dust cloud'. This procedure was repeated 28 times for 28 different values of t_0. Finally, the obtained separate particular dust clouds were summed up, resulting in the 'summed dust cloud'.

In the motion equation (2) of the particle, we considered only the gravitational forces of the three massive bodies and neglected forces induced by the radial solar radiation pressure and the Poynting–Robertson (P–R) drag. Here we show that this neglect was correct. In an inertial reference system for a dust particle with geometric cross-section A, the P–R drag force $\underline{F}_{P-R}$ and the radiation pressure force $\underline{F}_{rad}$ can be written as follows (Burns, Lamy & Soter 1979; Liou, Zook & Jackson 1995):

$$\underline{F}_{P-R} = -\frac{SA}{c^2} Q_{pr} \underline{v}, \quad (3)$$

$$\underline{F}_{rad} = \frac{SA}{c} Q_{pr} \left(1 - \frac{\dot{r}}{c}\right) \underline{\dot{s}}. \quad (4)$$

Here, $\underline{v}$ is the velocity vector of the particle, S, c and Q_{pr} are the solar energy flux density, the speed of light in vacuum and the radiation pressure coefficient, respectively, while $\underline{\dot{s}}$ is the unit vector in the direction of the Sun and $\dot{r}$ is the particle's radial velocity. Burns et al. (1979) and Liou et al. (1995) investigated the ratio of the radiation pressure force and the solar gravitation force and they stated that for particles with sizes greater than a few μm the radiation pressure force is negligible. However, very small particles (with a radius of less than 0.01 μm) are unaffected by the solar radiation, because the characteristic radiation wavelength is relatively too large to sustain absorption or scattering. The radiation pressure is maximal (and for certain materials may exceed the gravitational force) for particles with a radius in the range 0.1–0.5μm. Therefore, we calculated the gravitational force $\underline{F}_{gr}$ of the Sun, Earth and Moon, and the sum of

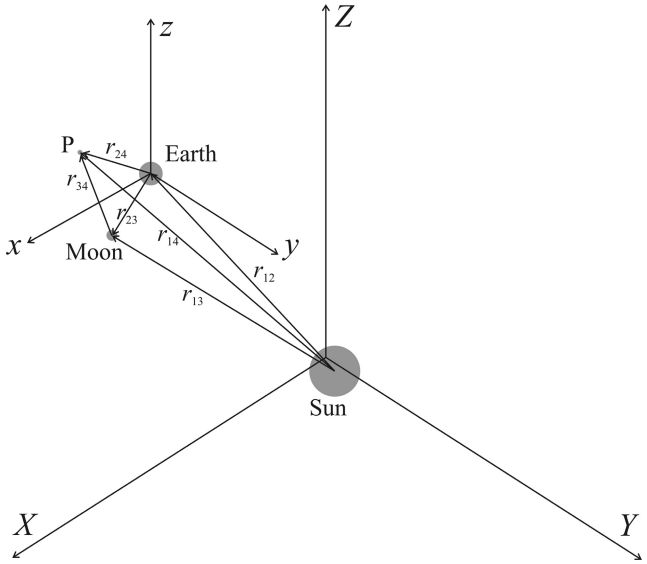

Figure 1. Position vectors of the components – Sun, Earth, Moon and particle (P) – of the studied four-body problem in the barycentric ecliptic coordinate system. The x–y plane is the plane of the ecliptic, the x- axis points towards the vernal equinox, $\boldsymbol{r}_{12}, \boldsymbol{r}_{13}, \boldsymbol{r}_{14}, \boldsymbol{r}_{23}, \boldsymbol{r}_{24}$ and $\boldsymbol{r}_{34}$ denote the vectors of the Sun–Earth, Sun–Moon, Sun–particle, Earth–Moon, Earth–particle and Moon–particle, respectively. The particle is in the vicinity domain V around the L5 Lagrange point. The sizes and distances are not to scale.

Table 1. The vicinity domain V, where $x_{0,L5}$, $y_{0,L5}$, $z_{0,L5}$, $v_{x0,L5}$, $v_{y0,L5}$ and $v_{z0,L5}$ denote the calculated initial position and velocity coordinates of the L5 Lagrange point at t_0. The size of the domain where the test particles are started is $0.0008 \times 0.0008 \times 0.0008$ in position and $0.00006 \times 0.00006 \times 0.000006$ in velocity range around L5. For units, see the text.

x_0	y_0	z_0
$\{x_{0,L5} - 0.0004, x_{0,L5} + 0.0004\}$	$\{y_{0,L5} - 0.0004, y_{0,L5} + 0.0004\}$	$\{z_{0,L5} - 0.0004, z_{0,L5} + 0.0004\}$
v_{x0}	v_{y0}	v_{z0}
$\{v_{x0,L5} - 0.00003, v_{x0,L5} + 0.00003\}$	$\{v_{y0,L5} - 0.00003, v_{y0,L5} + 0.00003\}$	$\{v_{z0,L5} - 0.000003, v_{z0,L5} + 0.000003\}$

the P–R drag force $\underline{F}_{P-R}$ and the radiation pressure force $\underline{F}_{rad}$ around this particle size range.

3 RESULTS

In the case of a particle with medium density $\rho = 3000$ kg m^{-3}, the value of Q_{pr} is 1 (Burns et al. 1979). The solar energy flux density at 1 au from the Sun is $S = 1.361$ kW m^{-2}. Using these numerical values, we started our simulation at 01:14 (UT) on 2017 August 19 (Fig. 2) and calculated the above-mentioned forces. According to Fig. 2, over the particle mass $m = 10^{-14}$ kg and particle radius $r = 1$ μm, the gravitational force dominates, which is consistent with the earlier finding of Burns et al. (1979).

Hence, we find that both the radiation pressure and the P–R drag are negligible relative to the gravitational force for particles with a radius over about 1 μm, whereas particles with a radius between 0.1 and 0.5 μm can be ejected from the vicinity area of the L5 point after a long enough period (Burns et al. 1979). Thus, it was correct not to take into consideration the radiation pressure and the P–R drag forces in our short-term simulations.

For a better understanding of the properties of the trapped particles around the L5 point, two types of simulations were performed. On the one hand, we studied the behaviour of a particular dust cloud versus time (Fig. 3) and, on the other hand, we investigated the summed dust cloud cumulated from 28 particular dust clouds (Fig. 4).

Fig. 3(a) shows the initial positions of the non-escaped particles (particular dust cloud) for 3650 d around L5 starting at $t_0 = 01{:}14$ (UT) on 2007 August 22 (Table 2) from the vicinity domain V. The particles starting with different velocities compose a band structure.

Fig. 3(b) displays the particular dust cloud around L5 containing the same trapped particles, 28 d later at 01:14 on 2007 September 19. The particles did not leave the vicinity of L5, the band structure is still discernible, but the particular dust cloud dispersed and became more homogeneous.

Fig. 3(c) illustrates the particular dust cloud around L5 containing the same trapped particles, 1460 d (4 yr) later at 01:14 on 2011 August 22. The particles form a U-shaped diffuse cloud with two wings directed opposite to the direction of rotation. The L5 point is still within the cloud.

Fig. 3(d) depicts the particular dust cloud around L5 containing the same trapped particles, 3650 d (10 yr) later at 01:14 on 2017 August 19. The L5 point is just at the leading edge of the elongated cloud having a long comet-like trail of broken-off particles. The ending (target) time 01:14 on 2017 August 19 of the simulations shown in Figs 3(d) and 4 was chosen to match the date of the imaging polarimetric patterns presented in the second part of this paper (Slíz-Balogh, Barta & Horváth 2018).

Fig. 4 shows a summed dust cloud composed of 28 particular dust clouds formed daily between $t_0 = 01{:}14$ on July 22 and $t_0 = 01{:}14$ on 2017 August 19. Similarly to Fig. 3(d), a comet-like trail of broken-off particles can be easily observed. The par-

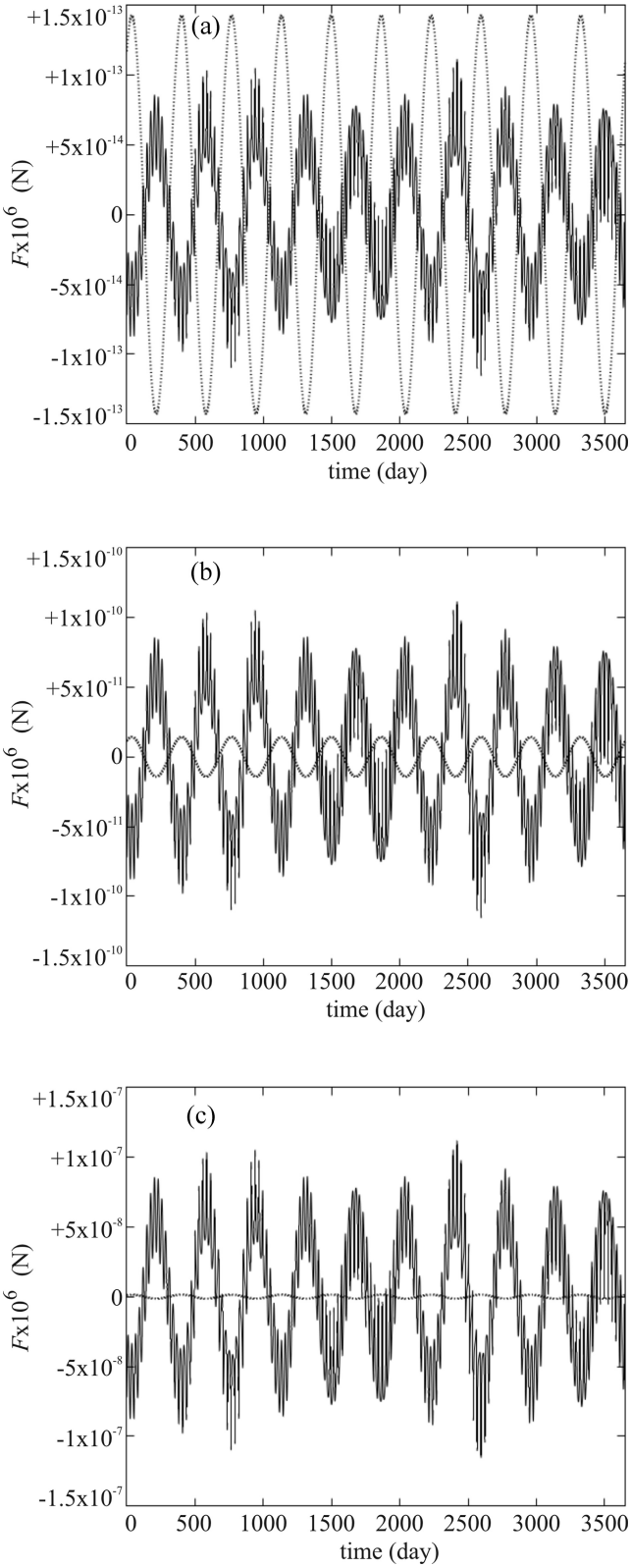

Figure 2. The gravitational force $\underline{F}_{\rm gr}$ of the Sun, Earth and Moon (continuous curve) and the sum of the P–R drag force $\underline{F}_{\rm P-R}$ and the radiation pressure force $\underline{F}_{\rm rad}$ (dotted curve) in the x-direction for a particle with mass m and radius r: (a) $m = 10^{-17}$ kg, $r = 0.1$ μm; (b) $m = 10^{-14}$ kg, $r = 1$ μm; (c) $m = 10^{-11}$ kg, $r = 10$ μm. The situation is similar in the y-direction, while in the z- direction $\underline{F}_{\rm gr}$ always is larger than $\underline{F}_{\rm P-R} + \underline{F}_{\rm rad}$.

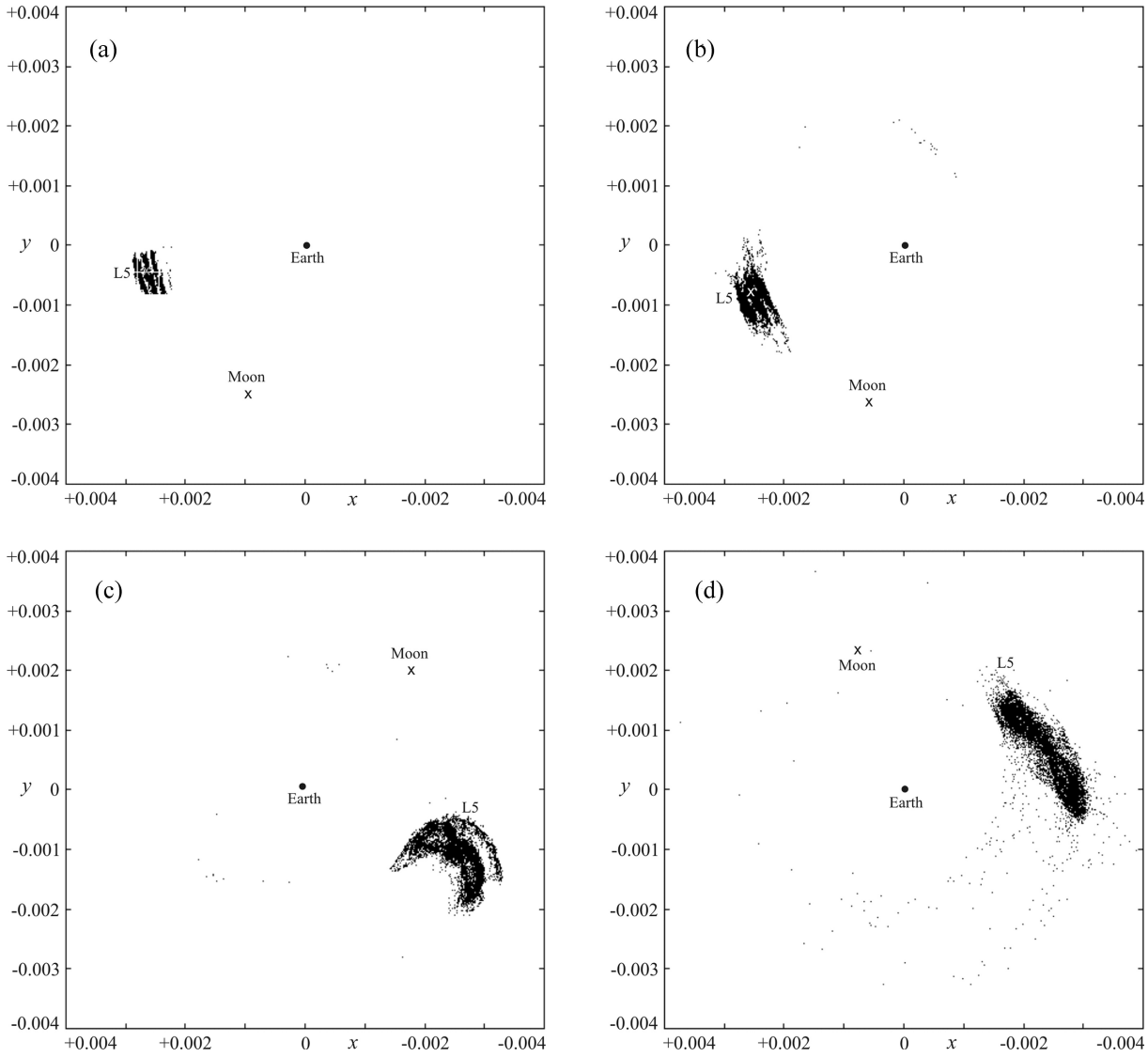

Figure 3. (a) Initial positions (black pixels) of the non-escaped trajectories of 1 860 000 particles started at $t_0 = 01{:}14$ (UT) on 2007 August 22 from the vicinity domain V around the L5 point in the geocentric ecliptic coordinate system. (b)–(d) The positions (black pixels) of these particles (composing a particular dust cloud) after 28 d (b), 1460 d (c) and 3650 d (d). Earth is denoted by a dot (in the centre of the plot), and the L5 point and the Moon are denoted by ×. A given black pixel means that in that direction of view there is at least one particle.

ticles forming some faint arcs were trapped from the edges of the vicinity domain V. The dimension of the summed dust cloud in the z-direction is approximately half of that in the x- or y-direction.

Fig. 5 shows the grey-coded particle density of the summed dust cloud. Depending on how many days earlier the particular dust cloud was trapped before the target date, two different types of structure can be distinguished. (i) Fig. 5(a) shows the summed dust cloud at the target date 01:14 on 2017 August 19 with particles trapped 1–28 d earlier. (ii) Fig. 5(b) shows the summed dust cloud at the target date 01:14 on 2017 August 19 with particles trapped 1–5, 8–18 and 21–28 d earlier. This cloud has a characteristic band structure around the L5 point with at least six bands. (iii) Fig. 5(c) displays the summed dust cloud with particles that were trapped 6, 7, 19 and 20 d earlier. The cigar-like/elongated shape of this cloud is totally different from that in Fig. 5(a).

The phenomenon of contraction is better seen in Fig. 6, which shows the contraction of three particular dust clouds (consisting of the orbits of 927 particles) in the z-direction about 6–7 and 19–20 d after the starting time (23:00 on 2017 July 28, August 1 and August 7). The orbit of each particle is sinusoidal also in the z-direction with the same period as that in directions x and y coinciding with the lunar orbital period. For all three particular dust clouds, the same phenomenon has been experienced.

4 DISCUSSION

In special cases, there are exact well-known classic analytical solutions of the three-body problem (Szebehely 1967; Rajnai, Nagy & Érdi 2014). Recently, a new exact solution of a special case of the four-body problem was discovered (Érdi & Czirják 2016). However, the general and, in particular, the 3D four-body problem can be solved only numerically.

The stability of the L4 and L5 Lagrange points of the Earth and Moon has some advantages that can be easily exploited. These points are suitable for spacecraft, satellite or space telescope parking

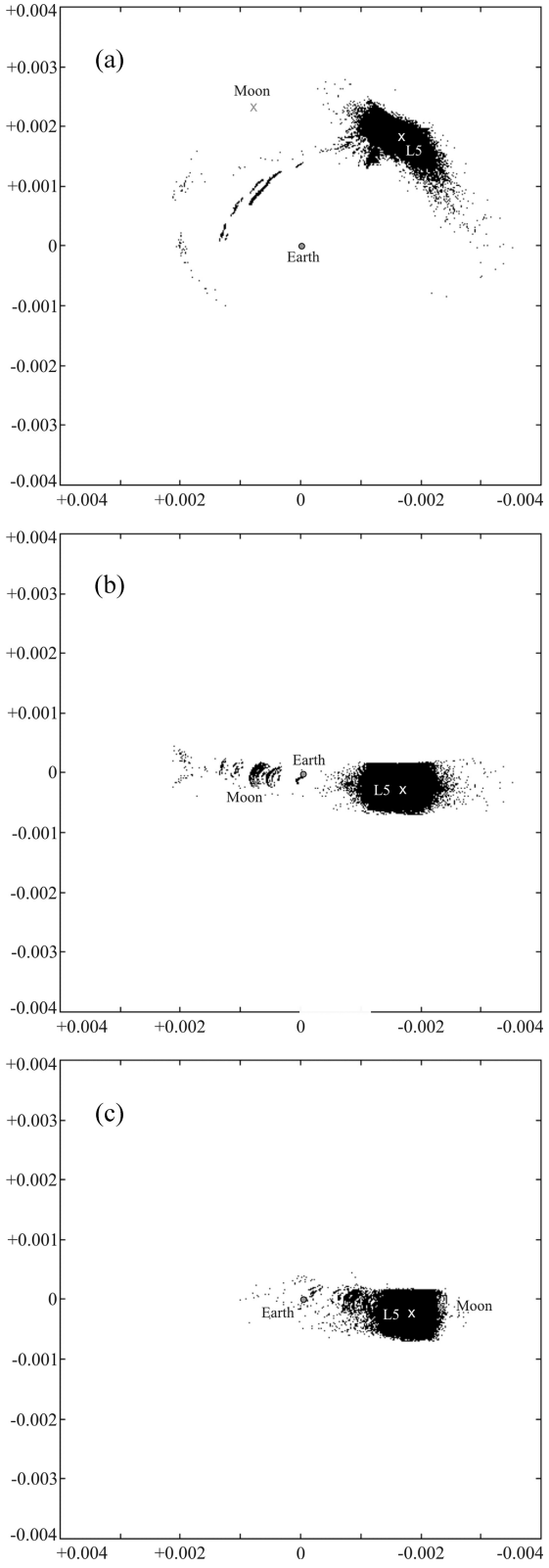

Figure 4. The summed dust cloud at 01:14 (UT) on 2017 August 19 in the geocentric ecliptic coordinate system in the *x*–*y* (a), *x*–*z* (b) and *y*–*z* (c) planes. The *x*-axis points towards the vernal equinox. The summed dust cloud is the combination of 28 separate particular dust clouds. The simulation of the 1st and 28th (last) particular dust cloud started at $t_0 = 01{:}14$ on 2017 July 22 and 01:14 on 2017 August 19, respectively. Earth is denoted by a grey dot (in the centre of the plot), the L5 point is denoted by a white $\times$ and the Moon is denoted by a grey $\times$. A given black pixel means that in that direction of view there is at least one particle.

Table 2. Initial positions and velocities of the Sun, Earth, Moon and the Lagrange point L5 for the epoch JD = 2 454 334.551 388 889 (t_0 = 01:14 on 2007 August 22) in the Solar system barycentric ecliptic coordinate system.

	Sun	Earth	Moon	L5
x_0	$9.890645064385753 \times 10^{-4}$	$8.634609584780867 \times 10^{-1}$	$8.625611534079515 \times 10^{-1}$	$8.600146967391559 \times 10^{-1}$
y_0	$4.795511121657655 \times 10^{-3}$	$-5.238211225876513 \times 10^{-1}$	$-5.263223250956695 \times 10^{-1}$	$-5.255959724119573 \times 10^{-1}$
z_0	$-8.461861578803593 \times 10^{-5}$	$-7.427675789134437 \times 10^{-5}$	$-3.194245021219622 \times 10^{-4}$	$-20.320528297276486 \times 10^{-5}$
v_{x0}	$-6.293333135136141 \times 10^{-6}$	$8.697706450830024 \times 10^{-3}$	$9.237525785409454 \times 10^{-3}$	$8.833349225711902 \times 10^{-3}$
v_{y0}	$1.782035107187389 \times 10^{-6}$	$1.460718375982933 \times 10^{-2}$	$1.443790508519941 \times 10^{-2}$	$1.404098840128974 \times 10^{-2}$
v_{z0}	$9.935326112885818 \times 10^{-8}$	$-2.250105040215131 \times 10^{-7}$	$4.852769975236783 \times 10^{-6}$	$-428.023679437153237 \times 10^{-7}$

with minimal fuel consumption (none the less, at the moment, there are no spacecraft orbiting at either L4 or L5 in the Solar system), or they can be applied as transfer stations for the mission to Mars or other planets, and/or to the interplanetary superhighway. The investigation of the dynamics of the Earth–Moon Lagrange points is also important from the point of view of space navigation safety. Because, when studying these points, the gravitational effect of the Sun cannot be ignored, it is necessary to study computationally a four-body problem, as we have done.

Figs 3 and 4 clearly depict the size and shape of the particular and summed dust clouds, but they do not give any information about the particle density. Therefore, we created images of the summed dust cloud (Fig. 5), where the picture area is uniformly divided into cells in the line of sight, and these cells are denoted with different shades of grey, depending on the number of particles in the cells. The structure of the summed dust cloud (Fig. 5a) consists of two distinct parts: (i) an extended, less-dense banded conglomerate (Fig. 5b) and (ii) an elongated denser one (Fig. 5c). The length of the bands of a particular dust cloud varies periodically (synchronous with the Moon's orbital period) depending on how many days earlier the particles were trapped. After being trapped, the particular dust cloud begins to contract in the band direction, and about 6–7 d later its length is minimal and its density is maximal. Then, it starts to expand again, and it reaches its maximal length after about another 6–7 d. If the trapping occurs 6, 7, 19 or 20 d earlier, the elongated and dense particular clouds will dominate (Figs 5a and c). If there were no trapping about 6, 7, 19 or 20 d earlier, then the summed dust cloud would look like that shown in Fig. 5b.

The lunar orbit's inclination with respect to the Earth's equator on 2017 August 19 is 19.°4, which is the same as the angle of the elongated cloud's axis from the horizontal (Fig. 5c). The angle of the band's axis from the vertical (Fig. 5b) is the same as the angle of the equator relative to the ecliptic (23.°44). This means that the bands of conglomerate are perpendicular to the ecliptic, while the elongated cloud is parallel to the lunar orbit plane (i.e. while the cloud is contracting, it is also twisting/slewing).

The phenomenon described in Fig. 6 is the periodic contraction of a particular dust cloud in the z-direction in the ecliptic coordinate system. Given that the motion of each particle of the dust cloud is chaotic (Slíz et al. 2015, 2017), supposedly a chaotic set is in the background of this phenomenon, but its explanation is not the subject of this paper.

Our simulations assumed steadily discontinuous material capture but, in reality, it is far from being so. For example, in the case of a meteor shower, the amount of trapped particles is larger, while at other times it can be much smaller. So, not all the bands in Fig. 5, which are the results of trappings of different numbers of days earlier with different velocities, are always present. Some bands might be missing, while others are more or less dense. The shape and structure of a summed dust cloud vary in a relatively short time, and they depend on the trapping date and the size of its particular dust clouds.

The imaging polarimetric patterns in the second part of this paper (Slíz-Balogh et al. 2018) confirm the structure of the KDC shown in Fig. 5(b). This remarkable similarity might mean that there was no significant particle trapping 6–7 or 19–20 d before the date of the polarimetric measurement.

The two types of summed dust clouds seen in Figs 5(b) and (c) show an interesting match with the two types of *Gegenschein* described by Moulton (1900): (i) a large and round cloud (Fig. 5b); (ii) a very much elongated cloud (Fig. 5c), varying on a time-scale of a few days, similar to our simulations.

Our simulations have shown that the dust particles trapped earlier than 20–25 d do not contribute to the dust cloud's structure, because after that time the dust is smoothly distributed. This also means that if we see bands, these are the results of trappings no earlier than 20–25 d.

We assume that our simulated particle conglomerate (summed dust cloud) around the L5 point (Fig. 5) corresponds to the dust cloud photographed by Kordylewski (1961). Salnikova et al. (2018) presented another computer model of the dust cloud formation around L5, and they also concluded that the accumulation of dust particles is indeed possible around L5.

Although our simulations were performed with a negligible (relative to the primaries) mass of the test particle, the results are the same for particles as massive as 10^6 kg (Slíz et al. 2015), if we disregard the gravitational interaction between the test particles. This means that even rock-sized objects can circulate along with the Lagrange point L5 for a long time.

The observation of the KDC with imaging polarimetry is more reliable than that with photometry. Thus, it can be imagined that the KDC did not reveal itself in the infrared patterns measured by the Infrared Astronomical Satellite (*IRAS*; https://lambda.gsfc.nasa.gov/product/iras/docs/exp.sup/toc.html) and the *Cosmic Background Explorer* (*COBE*; https://science.nasa.gov/missions/cobe), especially if astronomers did not search for it directly. Furthermore, because longer wavelengths are scattered less than shorter wavelengths and because the KDC can be detected by dust-scattered light, the photometric detection of the KDC is more difficult in the infrared than in the visible spectral range. Finally, the lack of photometric detection of the KDC by earlier astronomical missions (e.g. *IRAS*, *COBE*) does not exclude at all the existence of this dust cloud detected by us with imaging polarimetry (Slíz-Balogh et al. 2018). Note that the major aim of all earlier photometric missions was quite different from the detection of the KDC. If, during the evaluation of the registered photometric patterns of these missions,

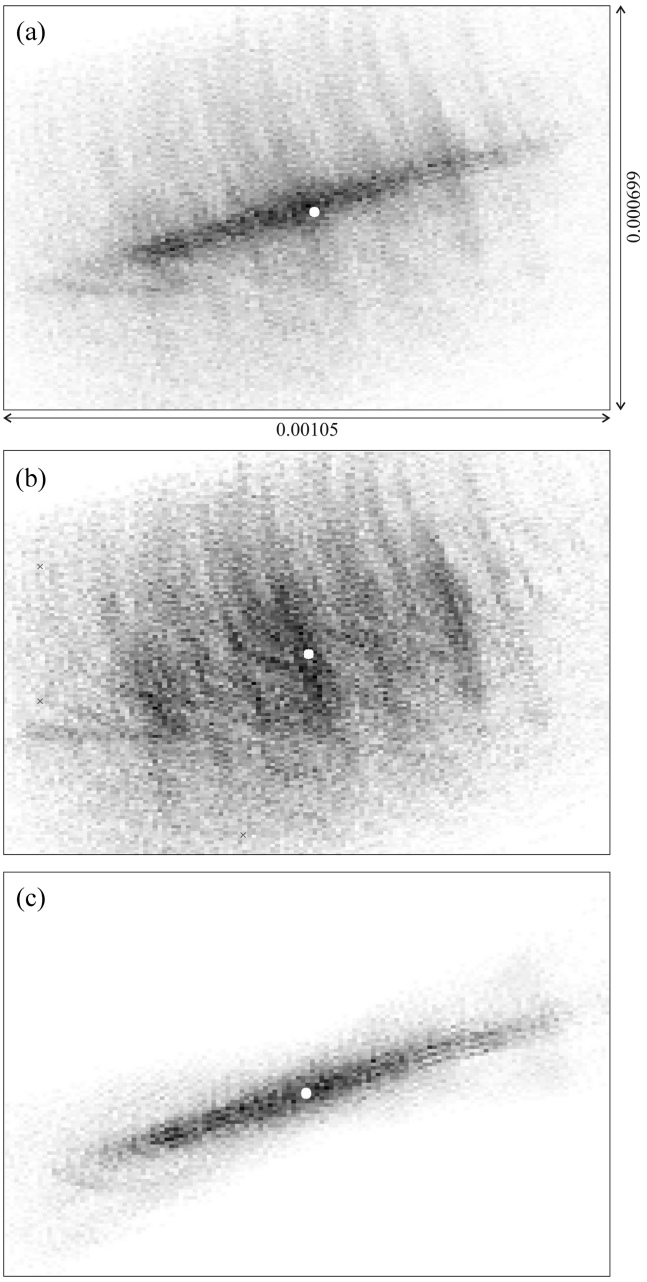

Figure 5. Computer-simulated density distribution of the particles of the KDC around the L5 point (white dot) of the Earth–Moon system in the equatorial coordinate system as we would see in the sky. The angular extension of the picture is $22\overset{\circ}{.}5$ (horizontal) $\times$ 15° (vertical). The horizontal and vertical axes denote the direction of the right ascension (RA) and the declination (Dec.), respectively. (a) Summed dust cloud (at target date 01:14 on 2017 August 19) of the particular dust clouds, the particles of which were trapped 1–28 d earlier. (b) As (a) but for particular dust clouds, the particles of which were trapped 1–5, 8–18 and 21–28 d earlier. (c) As (a) but for particular dust clouds, the particles of which were trapped 6, 7, 19 and 20 d earlier. The darker the shade of grey, the larger the particle density.

researchers did not look directly for the KDC, then the chance of its detection was considerably reduced, if not zero.

Something similar occurred with the detection of the fourth polarizationally neutral point of the Earth's atmosphere. The existence of this neutral point was predicted by David Brewster in the 1840s, after his discovery of the third neutral point, named after its first observer, Brewster (1842). However, the fourth neutral point can be observed only from higher altitudes ($>$ 1 km from the Earth's surface), a limitation that made such an observation difficult. Thus, the first scientifically documented observation of the fourth neutral point only occurred in 2002 (Horváth et al. 2002). Interestingly, in 2002, the satellite-born imaging polarimeter, called the *Polarization and Directionality of the Earth's Reflectances* (*POLDER*; Deschamps et al. 1994), had already been registering the polarization patterns of earthlight for several years. The polarization traces of the fourth neutral point should also exist in the polarimetric data of the *POLDER* mission. In spite of this, *POLDER* researchers did not recognize the fourth neutral point, because they did not seek it; they were interested in other aspects and meteorological applications of the *POLDER*-measured polarization data. However, if *POLDER* researchers were to have

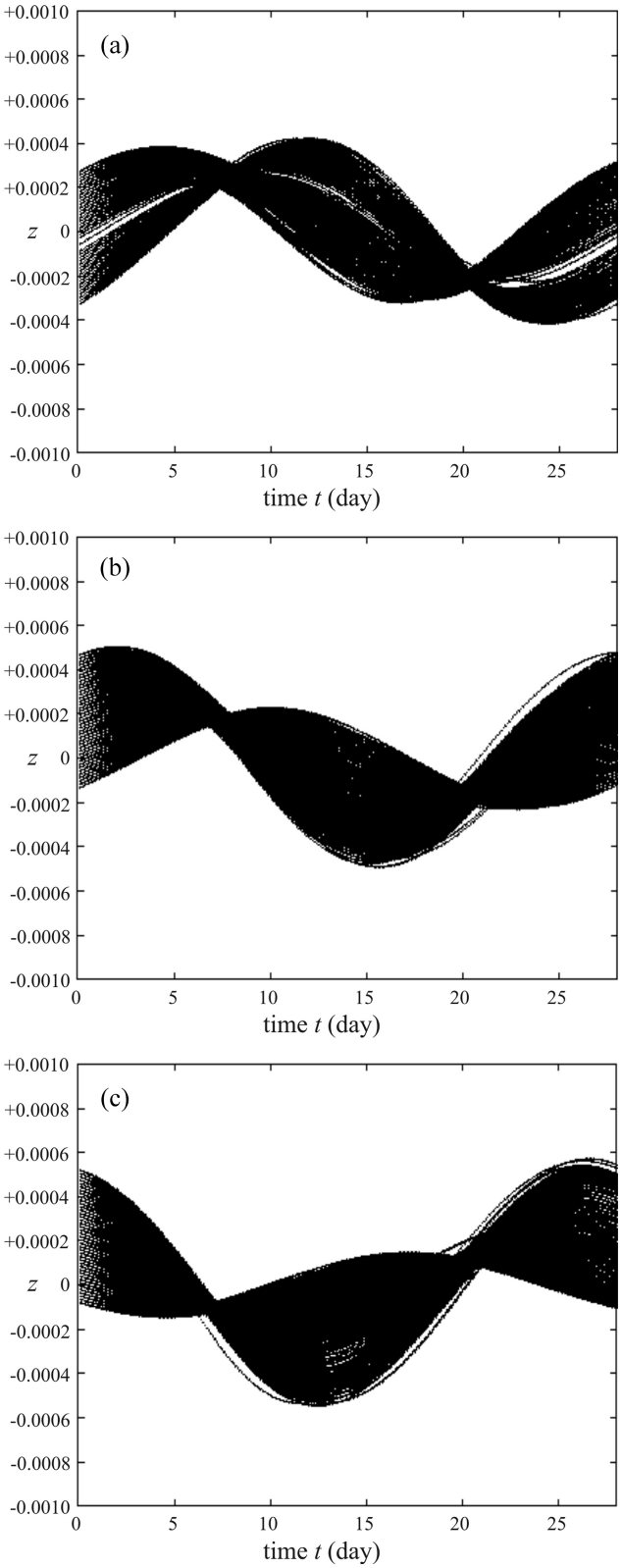

Figure 6. The z-coordinates of the particles of three particular dust clouds with different starting times t_0 versus time t from $t = 0$ to 28 d in the geocentric ecliptic coordinate system (see Fig. 1): (a) $t_0 = 23{:}00$ (UT) on 2017 July 28; (b) $t_0 = 23{:}00$ on 2017 August 1; (c) $t_0 = 23{:}00$ on 2017 August 7. In all three cases, in the z-direction, two contractions can be clearly seen after about 6–7 and 19–20 d. The particular dust cloud in (b) on August 8–9 and 20–21 shows an elongated, dense shape (Fig. 4c), whereas on the other days it has a less dense, banded form (Fig. 5b).

looked for the fourth neutral point, they surely would have found it in their polarization patterns measured from the high altitude of the *POLDER* satellite, as Horváth et al. (2002) found it in their polarization patterns measured from 3.5 km from a hot air balloon.

ACKNOWLEDGEMENTS

We are grateful to Miklós Slíz (software engineer, Graphisoft, Budapest, Hungary) for the development of the computer simulation software. We thank Tatiana Salnikova for her valuable comments on an earlier version of our manuscript.

Author contributions. Substantial contributions to conception and design: JSB, AB and GH. Performing experiments and data acquisition: JSB and AB. Data analysis and interpretation: JSB and GH. Drafting the article or revising it critically for important intellectual content: JSB and GH.

REFERENCES

Brewster D., 1842, Report of the 12th Meeting of the British Association for the Advancement of Science. J. Murray, London, p. 13
Burns J. A., Lamy P. L., Soter S., 1979, Icarus, 40, 1
Christou A., 2017, American Astronomical Society, DDA meeting, #48, 402.02
Deschamps P.-Y., Bréon F.-M., Leroy M., Podaire A., Bricaud A., Buriez J.-C., Séze G., 1994, IEEE Trans. Geosci. Remote Sensing, 32, 598
Érdi B., Czirják Z., 2016, Celestial Mechanics and Dynamical Astronomy, 125, 33
Fehlberg E., 1968, NASA Technical Report R-287
Horváth G., Bernáth B., Suhai B., Barta A., Wehner R., 2002, J. Opt. Soc. Amer. A, 19, 2085
John K. K., Graham L. D., Abell P. A., 2015, Lunar and Planetary Science Conference, 46, 2845
Kordylewski K., 1961, Acta Astron., 11, 165
Liou J. C., Zook H. A., Jackson A. A., 1995, Icarus, 116, 186
Moulton F. R., 1900, AJ, 21, 17
Murray C. D., Dermott S. F., 1999, Solar System Dynamics. Cambridge Univ. Press, Cambridge
Rajnai R., Nagy I., Érdi B., 2014, MNRAS, 443, 1988
Salnikova T., Stepanov S., Shuvalova A., 2018, Acta Astron., in press (https://doi.org/10.1016/j.actaastro.2017.12.022)
Schwarz R., Dvorak R., 2012, Celest Mech Dyn Astr, 113, 23
Schwarz R., Funk B., Bazsó Á., 2015, Orig. Life Evol. Biosph., 45, 469
Sheppard S. S., Trujillo C. A., 2006, Science, 313, 511
Slíz J., Süli Á., Kovács T., 2015, Astron. Nachr., 336, 23
Slíz J., Kovács T., Süli Á., 2017, Astron. Nachr., 338, 536
Slíz-Balogh J., Barta A., Horváth G., 2018, MNRAS, in press
Szebehely V., 1967, Theory of Orbits: The Restricted Problem of Three Bodies. Academic Press, New York

This paper has been typeset from a TEX/LATEX file prepared by the author.